Railroads Surface Crack detection using Active Thermography

Bilawal Ramzan
Graduate Student, Faculty of Mechanical Engineering
Ghulam Ishaq Khan Institute of Sciences and Technology (GIK)
Topi, Pakistan
gme1931@giki.edu.pk

Dr. Sohail Malik
Assisstant Professor, Faculty of Mechanical Engineering
Ghulam Ishaq Khan Institute of Sciences and Technology (GIK)
Topi, Pakistan
sohailmalik@giki.edu.pk

Dr. S.M. Ahmad
Professor, Faculty of Mechanical Engineering
Ghulam Ishaq Khan Institute of Sciences and Technology (GIK)
Topi, Pakistan
smahmad@giki.edu.pk

Milena Martarelli
Associate Professor, Department of Mechanical Engineering
University Polytechnics of Marche, Italy
m.martarelli@univpm.it

2021 International Bhurban Conference on Applied Sciences and Technologies (IBCAST) | 978-1-6654-0516-4/21/$31.00 ©2021 IEEE | DOI: 10.1109/IBCAST51254.2021.9393210

Abstract: ***Rails are basic mode of transportation all over the world. In-service railway lines are inspected for cracks on a prescribed frequency for damage diagnostics. The conventional methods of cracks detection of such large structure are either semi-automated or manual which make inspection process time consuming. Non-destructive testing utilizing infrared thermography has been proven additionally useful in structural health monitoring of various structures. Active thermography for the surface crack inspection of railroads is another potential application under exploration. In this work, lateral surface cracks of various dimensions are created on an in-service railroad. Railroad was uniformly heated to temperatures matching the practical conditions. For the crack detection, infrared camera was used to record the infrared radiation which were emitted as a result of applied thermal stimulus on rail road surface. As the surface temperature rises above the ambient condition, the railroad defects became prominent. Subsequently, post-processing was performed on raw infrared images to evaluate the results quantitively. The developed system will provide a robust and inexpensive solution for railway/highway authorities and NDT companies for damage diagnosis.***

The execution plan is given below:

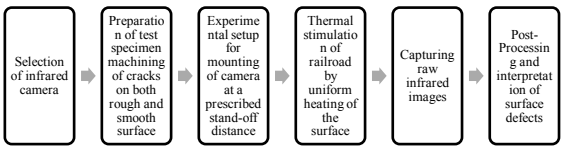

Keywords: ***Railroads, Thermography, Infrared, Radiations, Non-Destructive testing, Surface cracks, Creep failure, Uniform heating, Crack detection***

I. Introduction

With the increase in number of fast travelling rails and transporting heavier cargo than before; the rail network around the globe has been getting busier. Harsh environmental conditions and mechanical loading affect the integrity of railway structure considering that the ambient temperature in hotter regions of Pakistan may reach up to 50 ºC and an approximate load of 40 ton exerted by rail axle deployed on heavy haul routes. The major loading components due to vehicle weight generate bending, shear force and rolling contact pressure. Thermal stresses are also produced due to constrained elongation of welded rails along with residual stresses from in-field welding and manufacturing [1]. Distribution of stress in a rail track is illustrated in Figure 1.

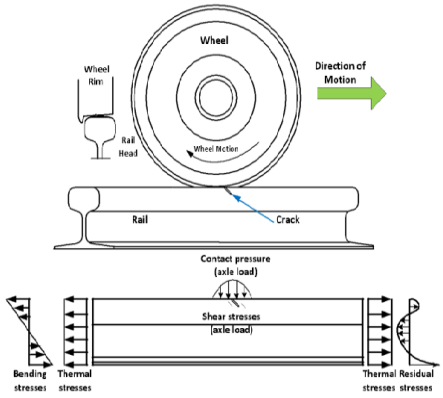

Figure 1 Contact of rail wheel and associated distribution of stress [2].

The composition parameters for manufacturing of rail steel are strictly monitored. For example, European rail standard grade steel 260 is composed of pearlitic microstructure with minor composition of ferrite at grain boundary. Traces of bainite, martensite and grain boundary cementite are not permitted [3][4]. For most operating temperature there is a probability of steel fracture in an event of abrupt material discontinuity (i.e. fatigue crack)

978-0-7381-0535-2/21/$31.00 ©2021 IEEE

in a brittle cleavage [5]. This strictly monitored characteristic of rail steel and manufacturing process infer that the possibility of the type defect to occur can be forecasted [3].

Most of the rail flaws that lead to catastrophic accidents causing rail breakage occur at rail head which are generated due to rail wheel contact [6]. Due to fatigue loading caused by rail-wheel contact rail head steel begins to deform plastically and cracks of various dimension and orientation start to appear. The different types of flaws produced at rail head include flaking, manufacturing defects (line), long groove, local battering and wheel or engine burns. A localised action by rolling wheel also generates creep forces at a contact patch of rail/wheel patch. These forces are longitudinal in nature; generated by traction of wheel on rail or as a result of sharp curve by compensating for different wheel diameters contacting the rail. Creep forces are also produced in lateral direction due to lateral oscillation of wheelset on the rail. It often causes wheel burn on rail due to continuous slippage of wheels on rail track [7]. The effect of creep is illustrated in figure 2.

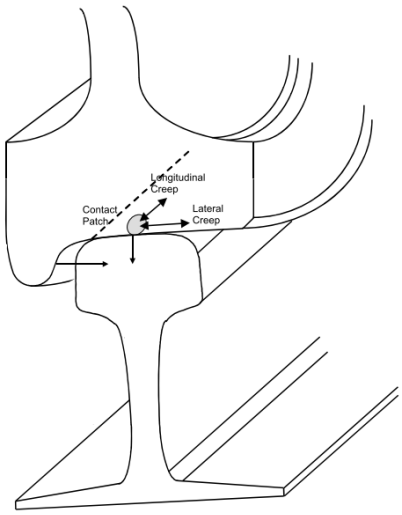

Figure 2 Longitudinal and lateral component of creep [7].

The cracks in railway line have been a perennial problem in Pakistan; which needs to be addressed at most attention with development of longest railway mass transit project under China Pakistan Economic Corridor (CPEC). The conventional inspection techniques for such a large rail network are either manual or semi-automatic which makes the whole inspection procedure time consuming.

The regular inspection of rails was initiated by Dr. Elemer Spery in USA back in 1920, for the inspection of crevices in rail [8]. Since then there has been a considerable R&D for inspection of early detection and cause of rail cracks including stress concentration cracks (SCC) and rolling contact fatigue (RCF) cracks. For this purpose, several non-destructive testing methods (NDTs) have been employed for detection of defects [9]. Commonly used NDT methods for the inspection of railway tracks include magnetic flux leakage testing (MFL), magnetic particle inspection, ultrasonic monitoring, visual or eddy current testing [10]. New high-speed NDE equipment has recently been developed, including high-speed cameras [11], Alternating Current Field Measurement probes (ACFM)[12]–[14], Electromagnetic Acoustic Transducers (EMATs)[15]–[18], Field Gradient Imaging (FGI)[19], ultrasonic phased arrays[20], and long-range ultrasonic, laser ultrasonic and multi-frequency eddy current sensors[21], acoustic sensors and infrared thermography[22]. The reliability of inspection methods for detecting cracks utilizing high energy laser or ultrasonic pulses was estimated by probability of detection concept (POD) and POD curves were introduced to justify the authenticity of inspection methods [23]–[25].

However, due to their clustered distributions and geometric interactions, it's difficult to characterize the rail head cracks. Compared to the above-mentioned NDT techniques, infrared thermography (IRT) with the benefit of non-contact sensing and simple visualization of small thermal variations is gaining the attention [26]–[32]. Depending on whether externally stimulated or self-radiating, IRT methods can be classified into active IRT and passive IRT. With the advantage of fast testing, hight temperature accuracy, real time/remote operation, representation of thermal images in 2D-contours, high SNR and emission of radiation within safe limits; active IRT is increasingly being used in a variety of applications [33]–[35].

Wilson [36] proposed to detect multiple cracks of rail rolling contact fatigue (RCF) by pulse eddy current (PEC) thermography. Cheng [37] and He[38] have 'lighted' and observed composite material damage from impact using eddy current pulse thermography (ECPT). He [39] tested the ECPT for corrosion blister detection in the mild steel. Li [40] used the ECPT in electrical modules for detection of bond wire state. Tian [41] applied the ECPT to assess the gear early on fatigue. Yin [42] reported on ECPT 's physical interpretation, and discussed the relations between mathematical and physical models. Gao [43] extracted spatial and time patterns based on the ECPT transient thermal sequences for automatic NDE. However, the problems with in-homogeneous heating, limited heating area and blocking effect of coil [41], [44] in ECPT reflective mode still challenge the accurate material and quantitative characterization of defects. Lahiri [23] recorded low frequency alternating magnetic field with wide area for thermo-graphic defect NDE. Jäckel [45] developed an external magnetic field electromagnet yokes to improve the contrast between crack detection by induction thermography. Netzelmann [46] developed a measuring device with induction generator scanning for inspection of rail surface defects at various velocities up to 15 km / h. Shepard [47] illustrated advancements and the study of pulsed thermographic data with improved spatial and temporal precision for identification of defects.

Recent studies in NDT of rail using active infrared thermography suggest that, still, there is no commercial product for the inspection rail head cracks. Therefore, the emphasis of this work is to detect transverse surface cracks, since they are very difficult to detect using traditional inspection systems. And to develop an inexpensive inspection system that is simple, easy to deploy and use, with minimal maintenance. All of these properties are demands of daily rail tracks inspection system nowadays. Advanced post-processing techniques are applied to the thermograms, and the effects are analysed using the signal-to - noise ratio (SNR).

II. Mathematical Modelling

A. Theoretical Background

All bodies, whether living or inert, above absolute zero temperature (-273.15 ºC) emit certain amount of electromagnetic radiations. The emitted radiation from an object surface is a function of its temperature and its relative efficiency thermal radiations, known as emissivity. This radiation, described as a set of discrete particles called "photons," is emitted across the whole electromagnetic spectrum whereas only Thermal InfraRed (TIR) band or Long-Wavelength InfraRed (LWIR) in IRT by utilizing a thermal sensor that is sensitive to a frequency interval of 2.1×10^{13} Hz to 4.3×10^{13} Hz at a wavelength of 7 μm to 14 μm [48]. The radiation emitted in that band of energy spectrum is called thermal radiation, and this band is chosen because of relation between the temperature value of an object and the radiation values emitted over the temperature spectrum from −73 °C to 125 °C is the highest in that band [49].

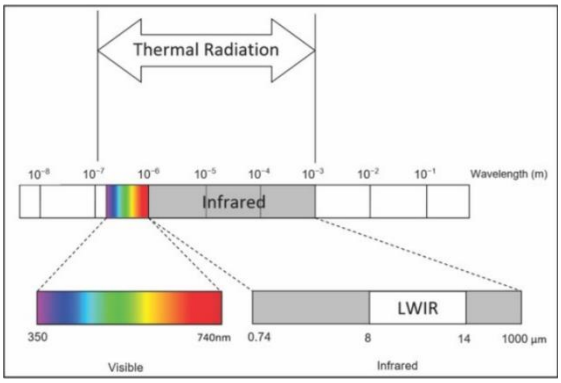

Figure 3 Spectrum of thermal radiations [50].

Thermal sensor measures the thermal radiation from the surface of an object, typically forming a sensor matrix and integrated inside a camera (thermographic / TIR camera), the IRT can measure the body's surface temperature value under examination using the Stefan-Boltzmann equation [51].

$$E = \epsilon\sigma T^4 \qquad 1$$

where E is thermal radiation emitted by real/grey body per unit area (W/m^2); ε is Emissivity of the grey body surface; σ is Stefan-Boltzmann's constant which is equal to

5.67×10^{-8} W/(m^2K^4) and T is the Absolute surface temperature of the grey body.

B. Governing equations

The governing equation for heat transfer through a material is given below:

$$-\left(\frac{\partial q_x}{\partial x}+\frac{\partial q_y}{\partial y}+\frac{\partial q_z}{\partial z}\right)+Q=\rho c\frac{\partial T}{\partial t} \qquad 2$$

In equation (2), q_x, q_y and q_z are heat flow components per unit area; ρ is the material density; c is the heat capacity of the material; Q represents the internal heat generation per unit volume; t denotes time and T is surface temperature of the object. Heat flow components can also be represented by using Fourier's law [52] as follows:

$$q_x=-k\frac{\partial T}{\partial x},\ q_y=-k\frac{\partial T}{\partial y},\ q_y=-k\frac{\partial T}{\partial z} \qquad 3$$

Where k is the coefficient of thermal conductivity.

By substituting the heat flow components to equation (2), governing equation for heat transfer can also defined as below:

$$\left[\frac{\partial}{\partial x}\left(k\frac{\partial T}{\partial x}\right)+\frac{\partial}{\partial y}\left(k\frac{\partial T}{\partial y}\right)+\frac{\partial}{\partial z}\left(k\frac{\partial T}{\partial z}\right)\right]+Q=\rho c\frac{\partial T}{\partial t} \qquad 4$$

The boundary conditions (BCs) to obtain a unique solution for the problem are stated below:

Specified Heat flow $$q_{s=}q_xn_x+q_yn_y+q_zn_z \qquad 5$$

Specified Temperature $$T_s=T(x,y,z,t) \qquad 6$$

Convection BC $$h(T_s-T_e)=q_xn_x+q_yn_y+q_zn_z \qquad 7$$

Radiation BC $$\epsilon\sigma T^4-\alpha q_r=q_xn_x+q_yn_y+q_zn_z \qquad 8$$

Here, n_x, n_y, and n_z denote direction cosines of outward normal to surface, T_s is the temperature of the surface, α is the coefficient of surface absorption, h is the coefficient of convection heat transfer at the surface and q_r is the component of radiation heat transfer per unit area.

It is worth noting that IRT only determines a body's surface temperature. Thus, IRT can only identify abnormal pathologies of the surface if the target is thermally excited during the acquisition process by means of artificial external thermal sources (active thermography) [53]. Otherwise, the captured thermal images cannot display interior regions, compensating with this other configuration (passive thermography) for greater simplicity and speed in superficial thermographic analysis.

III. Materials and Methodology

A. Testing Specimen

The sample we are studying is a standard 30lb rail section defined American Society of Civil Engineers (ASCE). This is flat bottom T-section steel rail which is used to construct railroads. The specimen is made of 880-grade rail sheets of steel. The number 880 represents the ultimate tensile strength i.e. 880 Mpa that can be applied to the sample and no failure will occur [54]. If we increase the load such that the stress at some point exceeds the ultimate strength, failure of the material will occur. The railway track sample is a bar with length much greater than that of its width and thickness. The dimensions of the testing specimen according to ASCE are given below [55]:

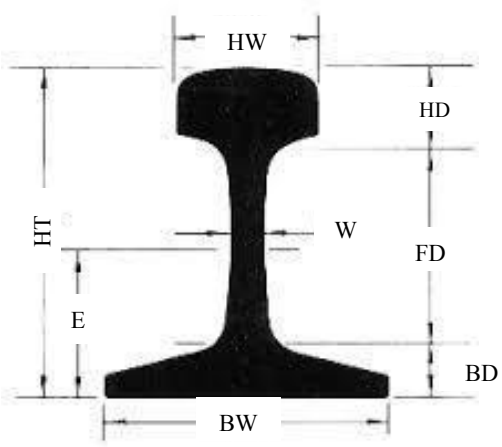

Figure 4 Dimensions of 30 lb ASCE rail section. Length L= 3.66m Width w = 0.7cm HW =4cm HD = 2.5cm E = 3.75cm FD = 4cm BD =
1.5cm BW = 7.5cm HT = 7.5cm.

Table 1 Chemical composition of specimen [56].

Chemical Composition	Weight percentage (% by mass)
Carbon	0.6-0.8
Manganese	0.8-1.13
Silicon	0.19-0.5
Sulphur	<0.035
Phosphorus	<0.035

Table 2 Mechanical properties of IRS 880 grade steel [56].

Mechanical properties	Value	Unit
Ultimate tensile strength	≥ 880	MPa
Percentage elongation	10%	-
BHN hardness	≥260	-

B. Artificial Cracks

Figure 5 shows the rail specimen used for experimental studies. The cracks were created on the railway surface at specific distance, unlike natural cracks rectangular slots were machined to simulate idealized wheel burn and manufacturing flaws due to RCF and creep forces[7] [57]. The railway specimen was divided in three parts; this division was made, so that, the results can be obtained when flaws on rail surface have different dimension and characteristics i.e. surface finish, crack depth etc. Transverse slots were machined across the rail head surface as artificial flaws. Slots depth varies from 0.5 mm to 2 mm while the length of longitudinal slots is between 20 to 30 mm; giving us a total of 8 slots of various size across the rail specimen. The opening of these slots (defect width) was maintained at 1 mm throughout the specimen. The geometric parameters of these artificial slots with respect to the type of surface are given in table 3. The transverse at rough and smooth surface are denoted as TF_{1R}-TF_{4R}, and TF_{1S}-TF_{4S} respectively as shown in Figure 5b and 5c. The different parts of the sample and their properties are as following:

- The first part of the sample is left as it is, since we have a used sample of railway track, the surface is very rough due to corrosion and wear. This portion will be used to analyse the effects of corrosion and surface roughness on thermographic data in the vicinity of surface flaw.
- The second part is done when the surface of the sample is ground with the help of a grinder, the difference between the first and second part is the surface finish only.
- The third part of the sample is made by creating the cracks on the surface. These cracks are across railhead and oriented in transverse direction.

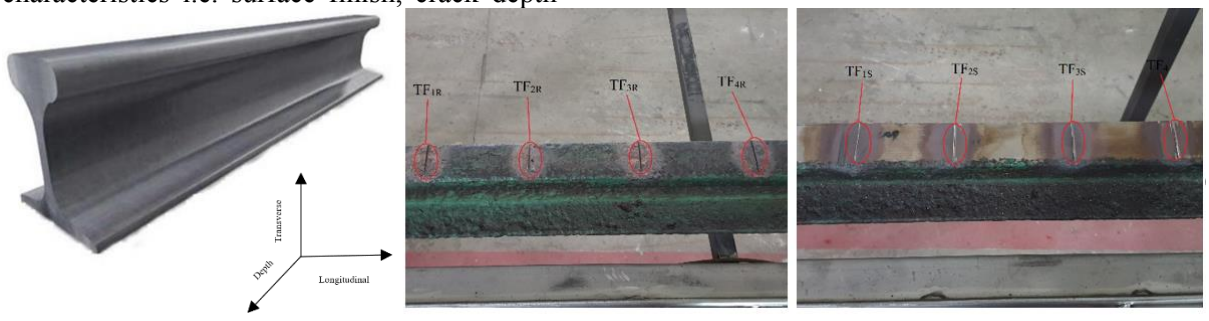

(a) (b) (c)

Figure 5 Rail specimen showing orientation of artificial slots on rough and smooth surface (a) Segment of rail track used for testing (b)Transverse Flaws on rough surface form TF_{1R} to TF_{4R} (c) Transverse flaws on smooth surface from TF_{1S} to TF_{4S}.

Table 3 Nomenclature and parameters for Artificial Flaws. Crack width is kept constant at 1 mm.

	Parameters								
Type of Surface	**Rough**				**Smooth**				
Nomenclature	TF_{1R}	TF_{2R}	TF_{3R}	TF_{4R}	TF_{1S}	TF_{2S}	TF_{3S}	TF_{4S}	Unit
Crack length	40	40	40	40	40	40	40	40	mm
Crack depth	0.5	1	1.5	2	0.5	1	1.5	2	mm

C. Characterization of Surface flaws

For the characterization of surface defects; time-based thermography technique was used by applying a uniform heat flux for a time interval on rail surface and monitoring the temperature distribution across the heated area by an infrared camera. Surface defects appear as local hot or cold areas on the contour plot in thermograms, since the defects interrupt the heat flow applied from the surface. Therefore, defects are identified in the captured infrared thermal images by detecting these inhomogeneous temperature regions.

It is important to highlight the underlying physical mechanism which results in the thermal signature of cracks. In order to understand this; let us consider Fourier's law by using Eq. (4)

$$\boldsymbol{q} = -k\left(\boldsymbol{i}\frac{\partial T}{\partial x} + \boldsymbol{j}\frac{\partial T}{\partial y} + \boldsymbol{k}\frac{\partial T}{\partial z}\right) = -k\nabla \boldsymbol{T} = \frac{1}{\boldsymbol{R_t}}\nabla \boldsymbol{T} \qquad 9$$

Where **q** is the applied flux on the rail surface, $\mathbf{R_t^{-1}}$ represents the thermal conductivity and **∇T** denotes the temperature gradient. As constant heat flux q applied to surface, localised thermal resistivity R_t at surface defect leads to a higher value of temperature gradient, or, in other words, a temperature distribution step, which can be used to detect surface flaws. In the case of three-dimensional heat conduction for inspection of in-service rail track with a localised source, q is not constant and, furthermore, R_t is affected. But the qualitative analysis from thermal images for the railhead surface defects is still possible. Consequently, higher R_t results in a decreased cooling and thus a higher maximum temperature while the heat is applied in the vicinity of a crack, which ultimately results in thermal crack signatures. Figure. 6 shows the schematic as well as configuration of setup for the inspection system.

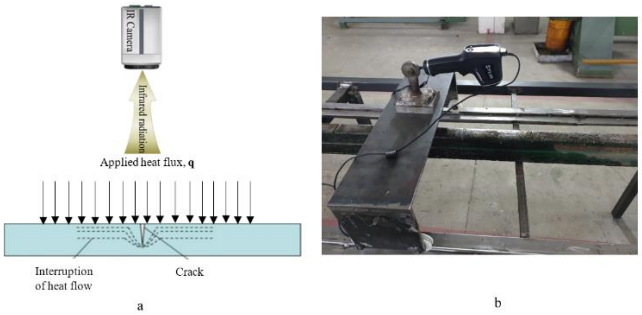

Figure 6 Configuration of thermography inspection system (a) Schematic diagram for thermography (b) Thermography inspection layout.

The experimental setup proposed in Figure. 6(b) consists of an infrared camera, rail track for the characterization of defects, rail track mounting platform and heating torch to heat flux to the surface. Thermal images produced due to applied thermal stimulus were captured using Flir TG165 infrared camera. Thermal stimulation is applied to heat the rail surface up to 76ºC. This type thermal heating used in the study of surface cracks can also be referred as short pulse. The thermal stimulation can last up to a few seconds while both heating and cooling rates are observed. Another important parameter for thermography of rail track is the selection of emissivity. The emissivity is the property of an object that indicates the radiations emitted by an object at specific temperature as compared to the black body. The summation of emissivity and resistivity for an opaque object is one. Therefore, highly emissive materials have low reflectivity due which infrared inspection is easier as high reflection causes noise in the images. The global emissivity of a railway track is 0.91, so, at this emissivity infrared inspection remains unaffected by reflection [58]. Since the inspection was performed in open environment the specimen was susceptible to temperature variation during capturing infrared images. Presence of noise in captured thermal images is ineheret as some thermal raditions also get scattered in the environment, therefore, post-processing is required to distinguish surface flaws and anamolies from sound area. Various post-processing methods have been devised to obtain a better signal to noise ratio) SNR.

However, for this study pulse phase thermograpghy (PPT) is prefered.

IV. Results and Discussion

Figure. 7 shows the captured infrared images and post-processed images for transverse flaws machined on a rough surface. Raw infrared images acquired using an infrared camera were post-processed to detect the cracks. Since the transverse crack has different temperature distribution as compared to the surrounded non-defective surface; that results in different cooling rates as R_t in defect vicinity produces greater temperature gradient. This phenomenon can be observed in thermal temperature histogram which shows the frequency of temperature distribution on rail surface. Another observation can also be made that after applying thermal stimulation for same time period the shallower defects cool at a rapid rate than deeper defects.

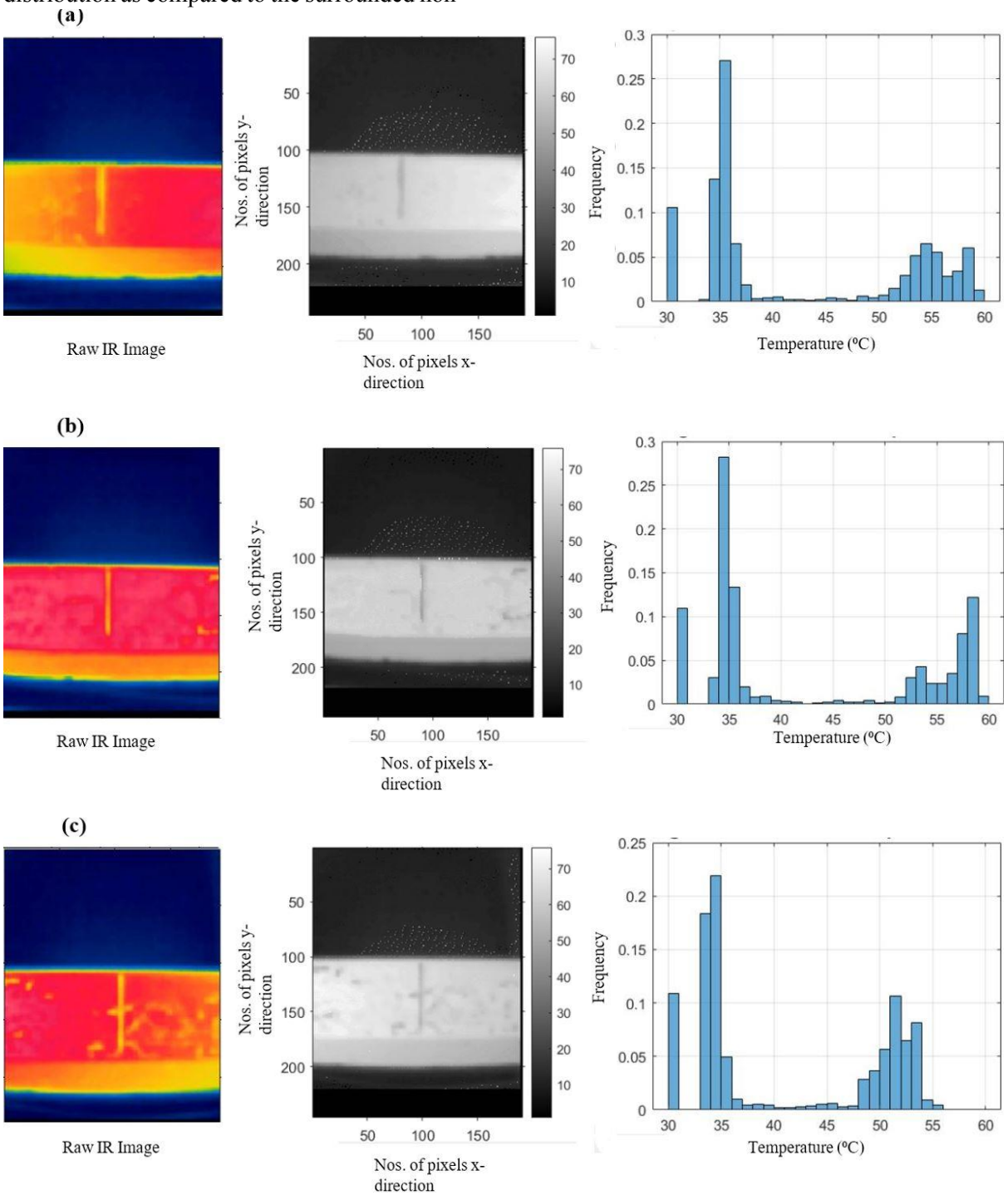

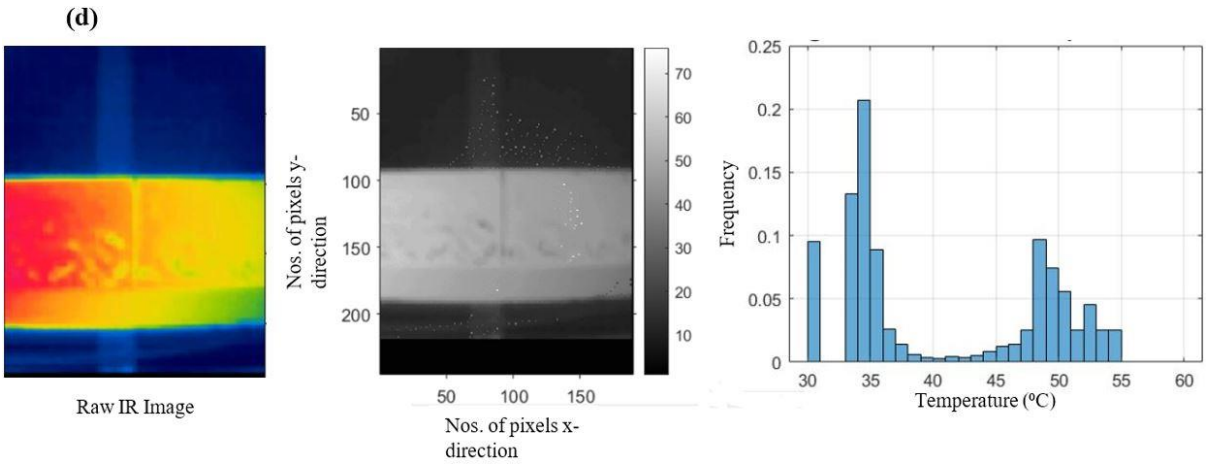

Figure 7 Active IRT for detection of transverse flaws on rough rail surface (a) Characterization of TF_{1R} through PPT and frequency of temperature distribution (b) Characterization of TF_{2R} through PPT and frequency of temperature distribution (c) Characterization of TF_{3R} through PPT and frequency of temperature distribution (d) Characterization of TF_{4R} through PPT and frequency of temperature distribution.

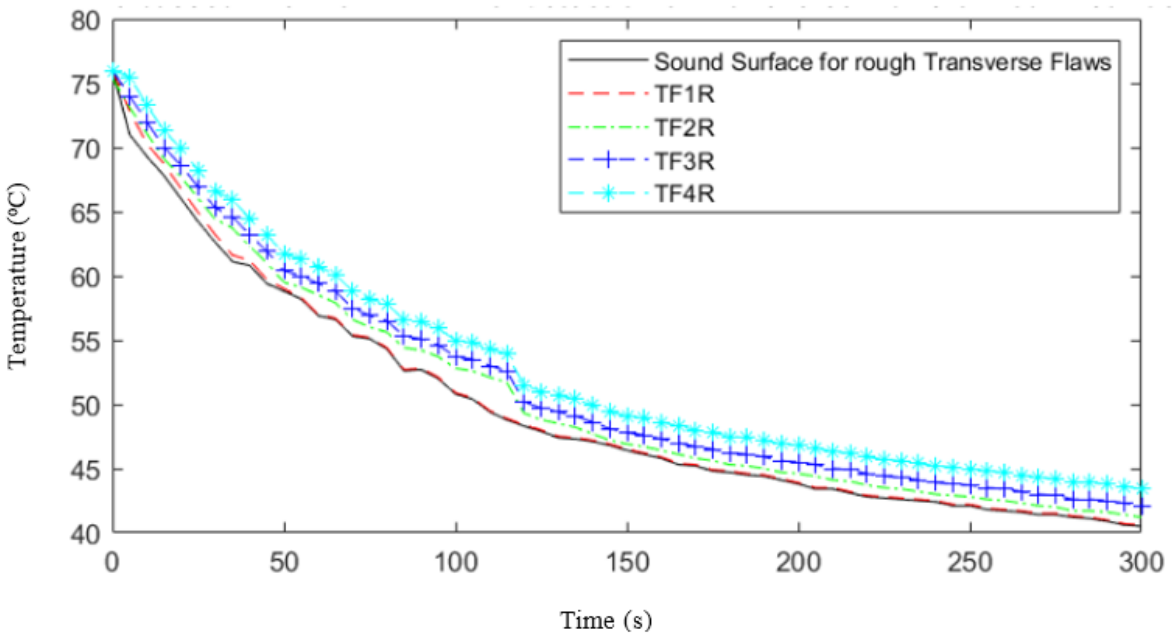

Figure 8 Time based thermography for the inspection of transverse flaws on rough rail surface.

As shown in Figure 7, the rail surface temperature was maintained between 50 ºC to 60 ºC during IRT, the contrast due to temperature distribution in defective area allows visible inspection of crack. The SNR for the detection of flaws further improves in post-processed images. PPT enhances the phase due to temperature gradient on the surface which enhances the visualization of thermal contrast not the defect. Since cooling rates and temperature gradient for flawed surface varies as compared to non-defective surface which produces a phase difference in thermograms and this phase difference assists in inspection of surface flaws. The frequency of temperature distribution in figure 7 for TF_{1R}, TF_{2R}, TF_{3R} and TF_{4R} characterizes the depth of flaws. In figure 7 (a), the depth of TF_{1R} is 0.5 mm which is shallower than other cracks of the same class have uniform temperature distribution of 56 ºC with surrounding sound surface. For TF_{2R}, figure 7 (b), the depth of crack is 1 mm and

thermal contrast of temperature distribution with sound surface is prominent at 61 ºC in thermal histogram. For TF_{3R} and TF_{4R}, in figure 7(c) and (d), the crack depths are 1.5 mm and 2 mm respectively, the frequency of recorded temperature for crack inspection shows a difference in temperature distribution for the surrounding non-defective surface. The difference in cooling rates for TF_{1R}, TF_{2R}, TF_{3R} and TF_{4R} are presented in figure 8. The graph establishes the fact that as the fact shallower defects cool at a rapid rate than deeper defects. It shows the decay rate for the transverse flaws heated to about 75 ºC. The temperature for each flaw is recorded at an interval of five seconds for five minutes and it can be observed that as the depth of defect increases at specific time interval the corresponding temperature is also greater the shallower defects for that same time interval.

Figure 9 shows results of active IRT performed on a polished surface. Artificial cracks machined on this surface have same dimension corresponding to transverse cracks on rough surface. In-service rail tracks face harsh environmental conditions and texture of rail surface varies depending upon the surrounding conditions. It is imperative to test whether the proposed technique works regardless of the environmental conditions. Post-processing of captured raw images were carried out to reduce environmental noise. Since the surface is smooth and there are no visible oxides or rust layers, therefore, tested surface prone to greater reflection of thermal radiations than the rusted surface. Thermograms in figure 9 show thermal contrast between sound and defective surface. Temperature gradient across the sound surface also varies due to increase reflection caused by reflective surface. The defects can be visualized in post-processed thermal images as shown in figure 9. The characterization of TF_{1S}, TF_{2S}, TF_{3S} and TF_{4S} has been made by the frequency of temperature distribution across the rail surface. It shows the difference in temperature distribution between defective and non-defective sounded surface. The cooling rates varies with crack depth; TF_{1S} cools faster than TF_{2S}, the effect is shown in frequency histogram for TF_{1S} and TF_{2S} in figure 9 (a) and (b) respectively.

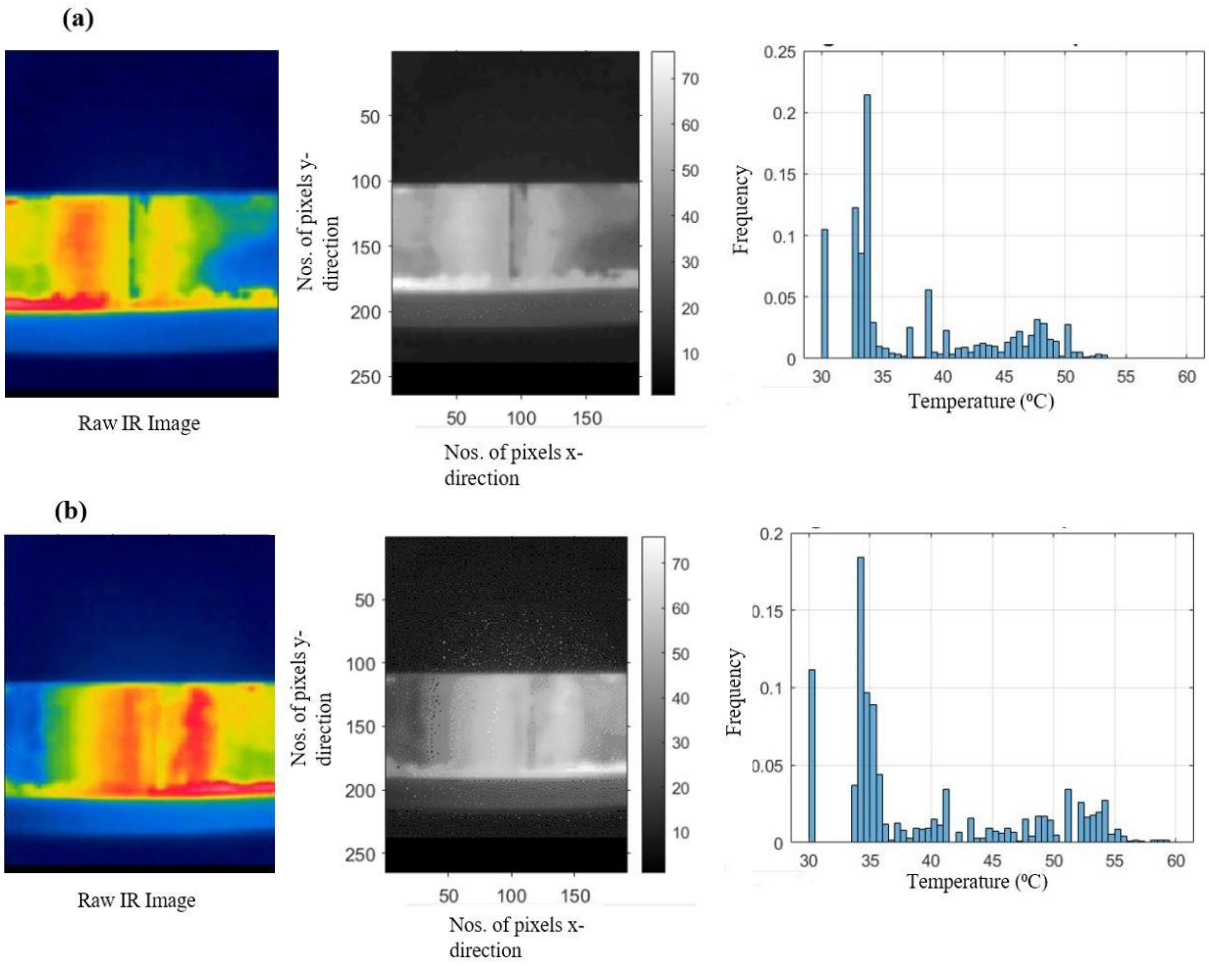

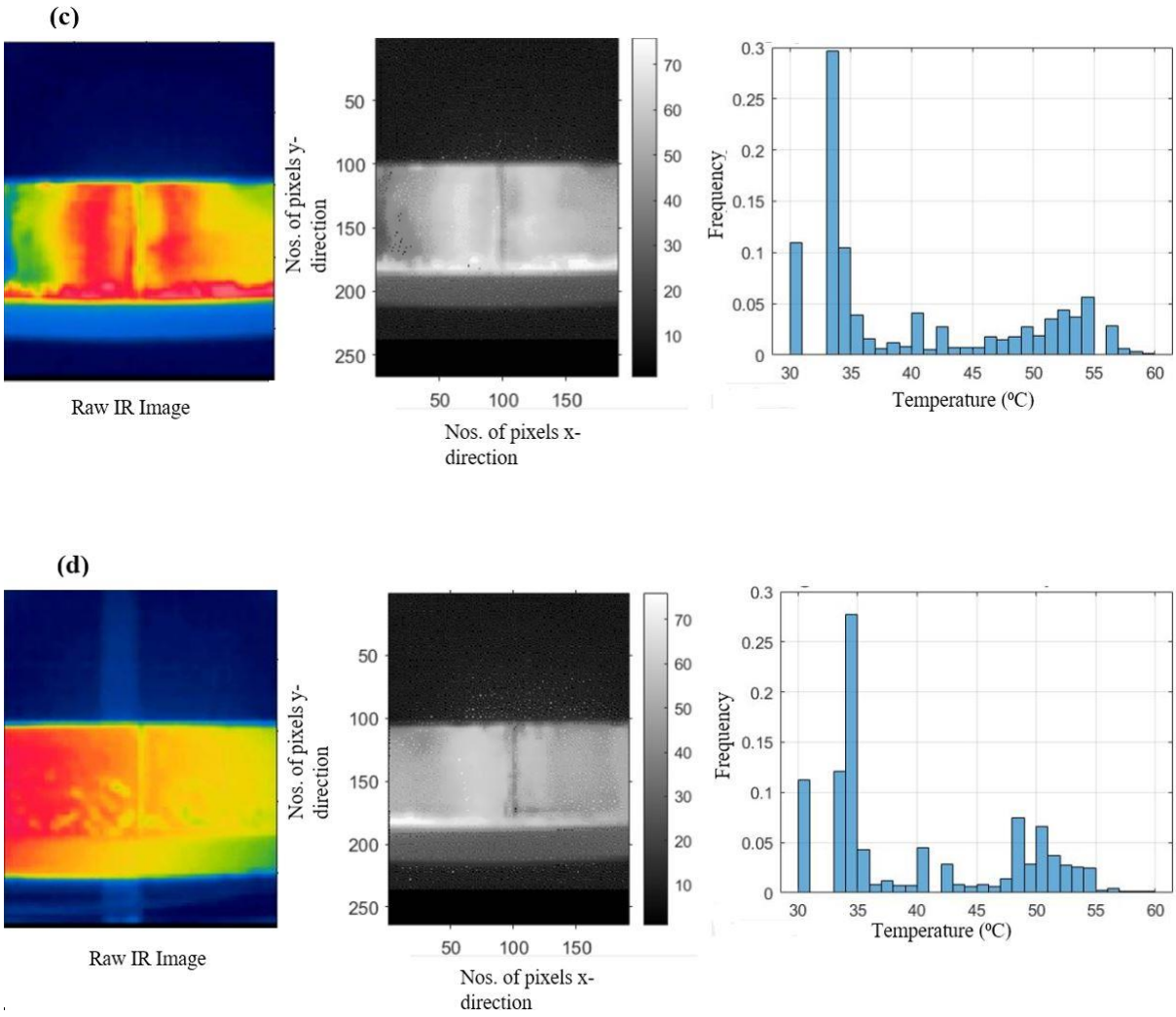

Figure 9 Active IRT for detection of transverse flaws on smooth rail surface (a) Characterization of TF_{1S} through PPT and frequency of temperature distribution (b) Characterization of TF_{2S} through PPT and frequency of temperature distribution (c) Characterization of TF_{3S} through PPT and frequency of temperature distribution (d) Characterization of TF_{4S} through PPT and frequency of temperature distribution.

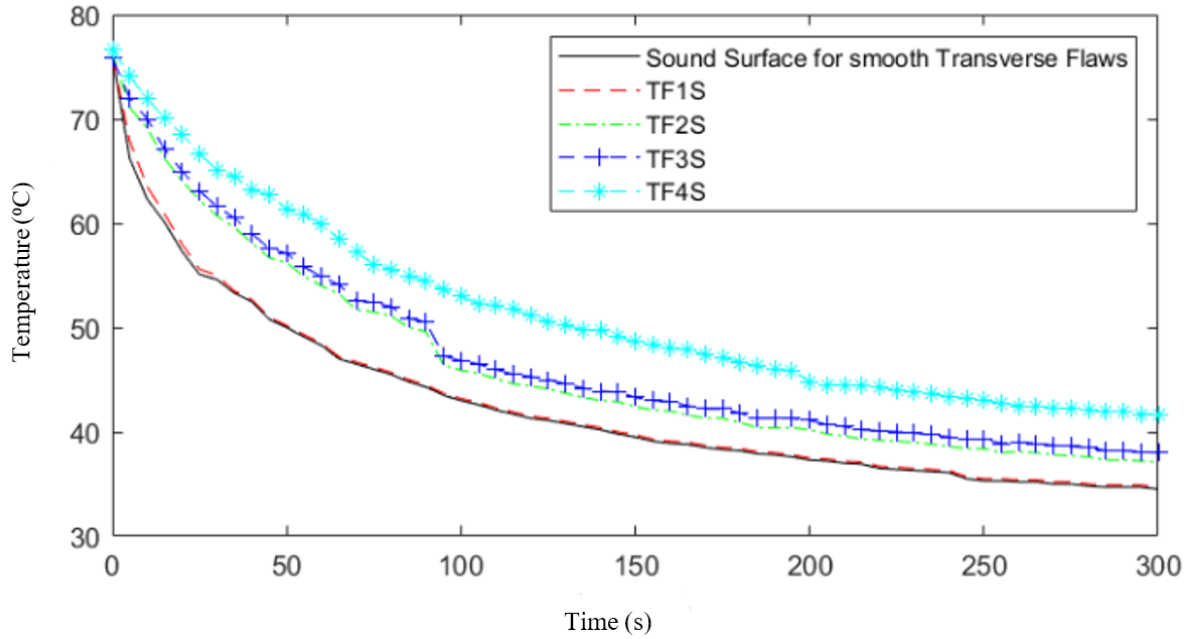

Figure 10 Time based thermography for the inspection of transverse flaws on smooth rail surface.

The cooling rates for TF_{1S}, TF_{2S}, TF_{3S} and TF_{4S} are depicted in figure 10. Overall decay pattern in figure 10 for transverse cracks on smooth surface resembles to that of rough surface cracks. The experimental parameters to record thermal data for both rough and smooth surface cracks were same. As shown in figure 10, as the depth of crack increase, subsequently, the cooling rates decreases. Comparison can be made between cooling rates for sound and defective surface. After five minutes of thermal stimulation the difference in cooling rates for all four cracks can be seen in time-based thermography graph shown above. The shallower crack is at 34.7 ºC which is coincident with temperature of non-defective surface, since the difference between surface and crack is 0.5 mm, whereas the temperatures for TF_{2S}, TF_{3S} and TF_{4S} are 37 ºC, 38 ºC and 41.7 ºC respectively.

V. Conclusion

Non-destructive testing utilizing active infrared thermography for inspection of cracks on rail surface proves to be a useful tool. It has been applied for detection of transverse flaws on rail track, the inspection of surface flaws on rail is crucial for the safety and reliable functioning of railway network. The feasibility of active infrared thermography for the detection of such defects is evaluated in this paper. Obtained results indicate that surface flaws can be identified by using active IRT. Post-processing was applied to enhance the visualization of defects, although the difference with respect to raw images is minimal. Further work is required to validate the findings with an expanded dataset of defects where it is possible to determine the most suitable heating configuration and to transform the inspection system to incorporate artificial intelligence for robust detection of flaws more efficiently.

Acknowledgments

The current research is supported by National Research Program for Universities (NRPU) Project number (10622/KPK/ NRPU/R&D/HEC/2017), HEC Pakistan.

References:

[1] U. Zerbst and S. Beretta, “Failure and damage tolerance aspects of railway components,” *Eng. Fail. Anal.*, vol. 18, no. 2, pp. 534–542, Mar. 2011, doi: 10.1016/j.engfailanal.2010.06.001.

[2] Y. D. Li, C. B. Liu, N. Xu, X. F. Wu, W. M. Guo, and J. B. Shi, “A failure study of the railway rail serviced for heavy cargo trains,” *Case Stud. Eng. Fail. Anal.*, vol. 1, no. 4, pp. 243–248, 2013, doi: 10.1016/j.csefa.2013.09.003.

[3] D. F. Cannon, K. O. Edel, S. L. Grassie, and K. Sawley, “Rail defects: An overview,” *Fatigue Fract. Eng. Mater. Struct.*, vol. 26, no. 10, pp. 865–886, Oct. 2003, doi: 10.1046/j.1460-2695.2003.00693.x.

[4] “PREN 13674-1 : DRAFT 2009 | RAILWAY APPLICATIONS - TRACK - RAIL - PART 1: VIGNOLE RAILWAY RAILS 46 KG/M AND ABOVE | NSAI.” [Online]. Available: https://shop.standards.ie/en-ie/Standards/PREN-13674-1-DRAFT-2009-346772_SAIG_CEN_CEN_792857/. [Accessed: 26-Aug-2020].

[5] Z. Andleeb *et al.*, “Multiphysics Analysis of CFRP Charpy Tests by varying Temperatures,” *Int. J. Multiphys.*, vol. 14, no. 2, pp. 143–160, Jun. 2020, doi: 10.21152/1750-9548.14.2.143.

[6] C. Bosomworth, Y. Q. Sun, M. Spiryagin, S. Alahakoon, and C. Cole, “Experimental investigation into the use of thermography for the detection of rail foot flaws,” in *ICRT 2017: Railway Development, Operations, and Maintenance - Proceedings of the 1st International Conference on Rail Transportation 2017*, 2018, vol. 2017-July, pp. 311–322, doi: 10.1061/9780784481257.031.

[7] A. Wilson and M. Kerr, “Rail Defects Handbook,” no. June 2012, pp. 1–83, 2012, doi:

http://extranet.artc.com.au/docs/eng/track-civil/guidelines/rail/RC2400.pdf.

[8] R. Clark, "Rail flaw detection: Overview and needs for future developments," in *NDT and E International*, 2004, vol. 37, no. 2, pp. 111–118, doi: 10.1016/j.ndteint.2003.06.002.

[9] J. L. Rose, C. M. Lee, T. R. Hay, Y. Cho, and I. K. Park, "RAIL INSPECTION WITH GUIDED WAVES," 2006.

[10] M. Raj, D. Mallik, S. Bansal, R. K. Saini, and R. K. Ajmeria, "Non-Destructive Testing and Inspection of Rails at JSPL-Ensuring Safety and Reliability."

[11] P. L. Mazzeo, M. Nitti, E. Stella, N. Ancona, and A. Distante, "An automatic inspection system for the hexagonal headed bolts detection in railway maintenance," in *IEEE Conference on Intelligent Transportation Systems, Proceedings, ITSC*, 2004, pp. 417–422, doi: 10.1109/itsc.2004.1398936.

[12] D. T.-N. D. TESTING and undefined 2005, "Recent developments and applications of the ACFM inspection method and ASCM stress measurement method," *AINDT-AUSTR INST OF …*.

[13] M. Howitt, "Bombardier brings ACFM into the rail industry Non-destructive testing in the rail industry View project Adiabatic CAES enabling renewables to power the grid View project," 2002.

[14] D. Topp and M. Smith, "Application of the ACFM inspection method to rail and rail vehicles," *Insight Non-Destructive Test. Cond. Monit.*, vol. 47, no. 6, pp. 354–357, Jun. 2005, doi: 10.1784/insi.47.6.354.66446.

[15] R. Edwards, S. Dixon, X. J.-N. & e International, and undefined 2006, "Characterisation of defects in the railhead using ultrasonic surface waves," *Elsevier*.

[16] R. Edwards, S. Dixon, X. J.-Ultrasonics, and undefined 2006, "Depth gauging of defects using low frequency wideband Rayleigh waves," *Elsevier*.

[17] R. Edwards, C. Holmes, … Y. F.-I.-N., and undefined 2008, "Ultrasonic detection of surface-breaking railhead defects," *ingentaconnect.com*.

[18] K. Mcaughey, M. Potter, … P. P.-18th W. C. on, and undefined 2012, "Rail track condition monitoring using electromagnetic acoustic transducers," *ndt.net*.

[19] M. Bentley, F. Lund, A. W.-N. I. Limited, undefined NSP1001, and undefined 2004, "Field Gradient Imaging technology, applications and solutions for component and structural integrity for track and rolling stock for the rail industry."

[20] G. Garcia and J. Zhang, "Application of ultrasonic phased arrays for rail flaw inspection," 2006.

[21] R. Shunmugam and K. Ramesh, "Modeling and Detecting Damage in Rails & Avoidance of Collision in the Tracks," vol. 2, no. 2, pp. 1–16, 2011.

[22] K. Bruzelius and D. Mba, "An initial investigation on the potential applicability of Acoustic Emission to rail track fault detection," *NDT E Int.*, vol. 37, no. 7, pp. 507–516, Oct. 2004, doi: 10.1016/j.ndteint.2004.02.001.

[23] B. B. Lahiri *et al.*, "Author's personal copy Infrared thermography based defect detection in ferromagnetic specimens using a low frequency alternating magnetic field," *Elsevier*, 2014, doi: 10.1016/j.infrared.2014.02.004.

[24] M. S. Malik, A. Cavuto, M. Martarelli, G. Pandarese, and G. M. Revel, "Reliability analysis of laser ultrasonics for train axle diagnostics based on model assisted POD curves," in *AIP Conference Proceedings*, 2014, vol. 1600, no. 1, pp. 396–404, doi: 10.1063/1.4879608.

[25] M. S. Malik, "Model assisted POD of laser-ultrasonics NDT for train axles: A

review," in *International Conference on Electrical, Electronics, and Optimization Techniques, ICEEOT 2016*, 2016, pp. 4645–4648, doi: 10.1109/ICEEOT.2016.7755600.

[26] R. Alfredo Osornio-Rios, J. A. Antonino-Daviu, and R. De Jesus Romero-Troncoso, "Recent industrial applications of infrared thermography: A review," *IEEE Trans. Ind. Informatics*, vol. 15, no. 2, pp. 615–625, Feb. 2019, doi: 10.1109/TII.2018.2884738.

[27] C. Meola, "Infrared thermography of masonry structures," *Infrared Phys. Technol.*, vol. 49, no. 3 SPEC. ISS., pp. 228–233, Jan. 2007, doi: 10.1016/j.infrared.2006.06.010.

[28] M. Manana, A. Arroyo, A. Ortiz, C. J. Renedo, S. Perez, and F. Delgado, "Field winding fault diagnosis in DC motors during manufacturing using thermal monitoring," in *Applied Thermal Engineering*, 2011, vol. 31, no. 5, pp. 978–983, doi: 10.1016/j.applthermaleng.2010.11.023.

[29] S. Stipetic, M. Kovacic, Z. Hanic, and M. Vrazic, "Measurement of excitation winding temperature on synchronous generator in rotation using infrared thermography," *IEEE Trans. Ind. Electron.*, vol. 59, no. 5, pp. 2288–2298, 2012, doi: 10.1109/TIE.2011.2158047.

[30] J. Zhu *et al.*, "Characterization of Rolling Contact Fatigue Cracks in Rails by Eddy Current Pulsed Thermography," *IEEE Trans. Ind. Informatics*, pp. 1–1, Jun. 2020, doi: 10.1109/tii.2020.3003335.

[31] Y. Hu, W. Cao, J. Ma, S. J. Finney, and D. Li, "Identifying PV module mismatch faults by a thermography-based temperature distribution analysis," *IEEE Trans. Device Mater. Reliab.*, vol. 14, no. 4, pp. 951–960, Dec. 2014, doi: 10.1109/TDMR.2014.2348195.

[32] D. B. Durocher and D. Loucks, "Infrared Windows Applied in Switchgear Assemblies: Taking Another Look," *IEEE Trans. Ind. Appl.*, vol. 51, no. 6, pp. 4868–4873, Nov. 2015, doi: 10.1109/TIA.2015.2456064.

[33] X. M.-M. Evaluation and undefined 2002, "Introduction to NDT by active infrared thermography," *w3.gel.ulaval.ca*.

[34] R. Usamentiaga, … Y. M.-I. T., and undefined 2018, "Automated dynamic inspection using active infrared thermography," *ieeexplore.ieee.org*.

[35] S. Doshvarpassand, C. Wu, X. W.-I. P. & Technology, and undefined 2019, "An overview of corrosion defect characterization using active infrared thermography," *Elsevier*.

[36] J. Wilson, G. Tian, I. Mukriz, and D. Almond, "PEC thermography for imaging multiple cracks from rolling contact fatigue," *NDT E Int.*, vol. 44, no. 6, pp. 505–512, 2011, doi: 10.1016/j.ndteint.2011.05.004.

[37] L. Cheng, B. Gao, G. Y. Tian, W. Lok Woo, and G. Berthiau, "Impact Damage Detection and Identification Using Eddy Current Pulsed Thermography Through Integration of PCA and ICA," *IEEE Sens. J.*, vol. 14, no. 5, p. 1655, 2014, doi: 10.1109/JSEN.2014.2301168.

[38] R. Yang and Y. He, "Eddy current pulsed phase thermography considering volumetric induction heating for delamination evaluation in carbon fiber reinforced polymers," *Appl. Phys. Lett.*, vol. 106, no. 23, Jun. 2015, doi: 10.1063/1.4922524.

[39] Y. He, G. Y. Tian, M. Pan, D. Chen, and H. Zhang, "An investigation into eddy current pulsed thermography for detection of corrosion blister," *Elsevier*, 2013, doi: 10.1016/j.corsci.2013.09.001.

[40] K. Li, G. Y. Tian, L. Cheng, A. Yin, W. Cao, and S. Crichton, "State detection of bond wires in IGBT modules using eddy current pulsed thermography," *IEEE Trans. Power*

Electron., vol. 29, no. 9, pp. 5000–5009, 2014, doi: 10.1109/TPEL.2013.2288334.

[41] B. Gao, Y. He, W. Woo, G. Tian, … J. L.-I. T. on, and undefined 2016, "Multidimensional tensor-based inductive thermography with multiple physical fields for offshore wind turbine gear inspection," *ieeexplore.ieee.org*.

[42] A. Yin, B. Gao, G. Y. Tian, W. L. Woo, and K. Li, "Physical interpretation and separation of eddy current pulsed thermography Related Articles Physical interpretation and separation of eddy current pulsed thermography," *Addit. Inf. J. Appl. Phys*, vol. 113, no. 6, p. 103907, Feb. 2013, doi: 10.1063/1.4790866.

[43] B. Gao, L. Bai, W. L. Woo, and G. Tian, "Thermography pattern analysis and separation Defect characterization by inductive heated thermography AIP Conf Integrated active transient thermography for rapid nondestructive analysis of sputtering target bond integrity," *Cit. Appl. Phys. Lett.*, vol. 104, no. 25, p. 1100, Jun. 2014, doi: 10.1063/1.4884644.

[44] J. Peng *et al.*, "Investigation into eddy current pulsed thermography for rolling contact fatigue detection and characterization," *Elsevier*.

[45] P. Jäckel and U. Netzelmann, "The influence of external magnetic fields on crack contrast in magnetic steel detected by induction thermography," *Quant. Infrared Thermogr. J.*, vol. 10, no. 2, pp. 237–247, 2013, doi: 10.1080/17686733.2013.852414.

[46] U. Netzelmann, G. Walle, S. Lugin, A. Ehlen, S. Bessert, and B. Valeske, "Induction thermography: principle, applications and first steps towards standardisation," *Quant. Infrared Thermogr. J.*, vol. 13, no. 2, pp. 170–181, Jul. 2016, doi: 10.1080/17686733.2016.1145842.

[47] S. S.-T. XXIII and undefined 2001, "Advances in pulsed thermography," *spiedigitallibrary.org*.

[48] S. Lagüela, L. Díaz-Vilariño, D. R.-N.-D. Techniques, and undefined 2016, "Infrared Thermography: Fundamentals and Applications," *books.google.com*.

[49] R. Usamentiaga, P. Venegas, J. Guerediaga, L. Vega, J. Molleda, and F. Bulnes, "Infrared Thermography for Temperature Measurement and Non-Destructive Testing," *Sensors*, vol. 14, no. 7, pp. 12305–12348, Jul. 2014, doi: 10.3390/s140712305.

[50] "Thermal Testing - Science." [Online]. Available: https://www.nde-ed.org/EducationResources/CommunityCollege/Other Methods/IRT/IR_Science.php. [Accessed: 01-Sep-2020].

[51] I. Garrido, S. Lagüela, and P. Arias, "Infrared Thermography's Application to Infrastructure Inspections," *Infrastructures*, vol. 3, no. 3, p. 35, Sep. 2018, doi: 10.3390/infrastructures3030035.

[52] D. Hahn and M. Özisik, *Heat conduction*. 2012.

[53] Z. Andleeb *et al.*, "Multiphysics Study of Infrared Thermography (IRT) Applications," *Int. J. Multiphys.*, vol. 14, no. 3, pp. 249–271, Sep. 2020, doi: 10.21152/1750-9548.14.3.249.

[54] M. Zhu, G. Xu, J. H. Zhou, R. M. Wang, and X. L. Gan, "Study on service performance of 880 MPa-grade and 980 MPa-grade rail steels," *IOP Conf. Ser. Mater. Sci. Eng.*, vol. 244, p. 012025, Sep. 2017, doi: 10.1088/1757-899x/244/1/012025.

[55] W. -Web, "Rail Sections HT-Height BW-Width of Base HW-Width of Head FD-Fishing BD-Depth of Base E-Bolt Hole Elevation."

[56] % Bhn, "Heavy haul tracks Specification Grade Chemical composition Mechanical properties % by mass Rm (MPa) Elongation," 2017.

[57] G. L. Nicholson, A. G. Kostryzhev, X. J. Hao, and C. L. Davis, "Modelling

and experimental measurements of idealised and light-moderate RCF cracks in rails using an ACFM sensor," *NDT E Int.*, vol. 44, no. 5, pp. 427–437, Sep. 2011, doi: 10.1016/j.ndteint.2011.04.003.

[58] R. Usamentiaga, S. Sfarra, J. Fleuret, B. Yousefi, and D. Garcia, "Rail inspection using active thermography to detect rolled-in material," pp. 1–8, 2018, doi: 10.21611/qirt.2018.107.